Design of integrated silicon waveguides for Raman-enhanced four-wave mixing in the telecom band

SHIYU SUN,* **GORAN Z. MASHANOVICH, AND ANNA C. PEACOCK**

Optoelectronics Research Centre, University of Southampton, Southampton SO17 1BJ, UK
*S.Sun@soton.ac.uk

Abstract: Silicon planar waveguides are designed to maximize the wavelength conversion efficiency via the use of Raman-enhanced four-wave mixing in the telecom band. By investigating the dispersion properties of various rib waveguide structures, the optimum etch depth and width are selected to obtain efficient phase-matching for a continuous-wave pump at 1545 nm. The design benefits from good fabrication tolerance in the structural parameters, which are well within the precision of standard lithography and etching processes. Using the optimized waveguides, simulations show that it is possible to reach conversion efficiencies as high as ~45 dB for waveguide lengths as short as 4.6 cm, with a pump power of only 130 mW. This enhancement in the conversion efficiency is about 50 dB higher than conventional values for FWM in integrated silicon photonic systems, highlighting the benefits of exploiting the coupling between the two nonlinear processes.

1. Introduction

Four-wave mixing (FWM) is an important nonlinear process that can be used to control and manipulate optical signals within integrated photonics platforms. Owing to the large third-order nonlinearity and high optical confinement, silicon waveguide systems are particularly well suited to the observation of FWM processes using continuous-wave (CW) pump sources with optical powers typically employed in communication systems [1]. Capitalizing on the compact and integrated geometries, silicon-based FWM has been exploited for high-speed and high-capacity data conversion [2] and regeneration [3]. However, without resorting to pulsed pump sources [4] or complex resonator geometries [5,6], the conversion efficiencies in these chip-based systems are typically very low (~ -30 dB), with the maximum value of ~ -10 dB obtained for a waveguide with very precise dispersion engineering [7].

A convenient approach to enhancing the conversion in FWM interactions is to couple the parametric nonlinear process with the resonant Raman response of the material. Raman-enhanced FWM (RE-FWM) has been explored in silicon systems for down-conversion of data signals using coherent anti-Stokes Raman scattering (CARS) processes [8], which converts Stokes photons into anti-Stokes photons under quasi-phase-matching conditions. However, as of to date the conversion efficiencies obtained via this process when using CW pump sources have been limited and, for example, the largest reported conversion of ~ -50 dB required a pump of 700 mW due to the strong phase mismatch [9]. Significantly, as the gain efficiency of Raman scattering is higher at the Stokes wavelength compared to the anti-Stokes, higher gains should be possible using a coherent Stokes Raman scattering (CSRS) process, where the signal is positioned at the anti-Stokes wavelength for up-conversion [10]. Indeed, RE-FWM of the Stokes signal has recently been demonstrated using a silicon core fiber structure, where it was shown that a

conversion efficiency of ∼ −44 dB was possible for a low power pump (28 mW), representing an enhancement of 15 dB, even for a non-phase-matched process [11]. With further optimization of the waveguide designs to achieve phase-matching, it is anticipated that large RE-FWM conversion efficiencies could be obtained with traditional CW pump sources.

In this paper, we investigate design parameters for integrated silicon waveguides to optimize the RE-FWM conversion of an anti-Stokes signal at 1430 nm, to the Stokes wave at 1680 nm, using a CW telecom band pump source at 1545 nm. Our work starts by considering the dispersion properties of different waveguide structures etched into silicon-on-insulator (SOI) platforms with silicon thicknesses of 220 nm and 500 nm. Comparison of the FWM bandwidths reveals that larger rib structures etched into the 500 nm silicon are preferable for maximizing the interaction with the Raman gain. Following selection of the optimal structure parameters to achieve efficient nonlinear conversion, the tolerances for the waveguide parameters such as width and etch depth are studied to validate the fabrication precision and the experimental feasibility. The simulation results indicate that a maximum conversion efficiency of about 45 dB is possible for a pump power of only 130 mW, which is more than 50 dB higher than the best results obtained for FWM conversion in optimized planar silicon waveguides.

2. Description of the nonlinear propagation

Figure 1(a) shows a schematic of the proposed setup for the observation of RE-FWM, where a CW pump source at λ_p = 1545 nm is coupled into a silicon waveguide together with a tunable signal λ_s. The nonlinear processes that contribute to RE-FWM are schematically illustrated in Fig. 1(b) and (c), where (1) is degenerate FWM, (2) is stimulated Raman scattering (SRS), and (3) is inverse Raman scattering (IRS). Here Fig. 1(b) corresponds to CSRS conversion and Fig. 1(c) is CARS. For CSRS, the Stokes light is originally generated by FWM, which is enhanced due to the existence of SRS. The compensation of the pump power as a result of IRS further enhances the Stokes light, which is what leads to the higher gains for this process. For CARS, the anti-Stokes light is generated by FWM with the assistance of phonons generated by SRS with the right energy and momentum.
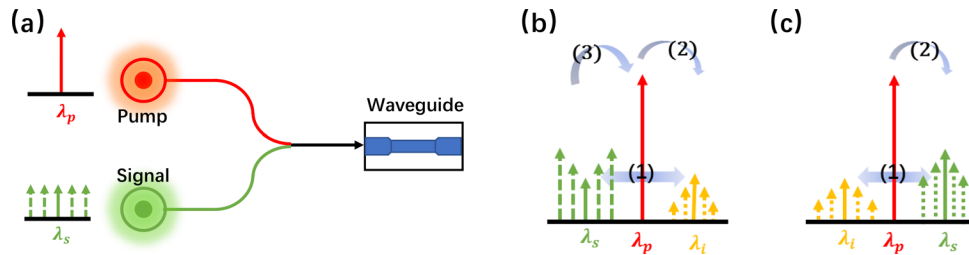

Fig. 1. (a) Schematic of the design of the experimental setup. (b) Schematic of the CSRS process. (c) Schematic of the CARS processes. In these images the arrows represent a transfer of energy via (1) FWM, (2) SRS and (3) IRS.

To quantitatively evaluate the nonlinear performance, the spectral evolution resulting from the nonlinear propagation is simulated using the nonlinear Schrödinger equation (NLSE) [12]:

$$\frac{\partial A}{\partial z} + \frac{\alpha}{2}A - i\sum_{n=1}^{\infty}\frac{i^n\beta_n}{n!}\frac{\partial^n A}{\partial t^n} - \frac{\sigma}{2}\left(1+i\mu\right)N_c A =$$
$$i\left(\gamma\left(\omega_0\right)+i\gamma_1\frac{\partial}{\partial t}\right)\left(A(z,t)\int_0^\infty R(t')\,|A(z,t-t')|^2\,dt'\right). \tag{1}$$

For the terms on the left-hand side of the equation, A is the pulse amplitude, α is the linear propagation loss, β_n is the nth order dispersive term, and σ ($\sigma = 1.45 \times 10^{-21}$ m^2 [13]) is

the free-carrier parameter, with μ and N_c representing the free-carrier dispersion and density, respectively. We note that dispersion terms up to the fourth-order (β_4) are included in our simulations as these are most important for determining the FWM phase matching. The terms on the right-hand side of Eq. (1) describe the nonlinear propagation, where γ is the nonlinearity parameter, $\gamma_1 = d\gamma/d\omega \approx \gamma/\omega_0$, and $R(t)$ is the nonlinear response function, including the delayed Raman contribution as given in [14]. Owing to the nonlinear absorption in silicon, γ is expressed in the form: $\gamma = k_0 n_2/A_{\text{eff}} + i\beta_{\text{TPA}}/(2A_{\text{eff}})$, in which k_0 is the propagation constant, n_2 ($n_2 = 5.5 \times 10^{-18}$ m^2/W at 1545 nm [14]) is the nonlinear refractive index, β_{TPA} ($\beta_{TPA} = 10 \times 10^{-12}$ m/W at 1545 nm) is the two-photon absorption (TPA) coefficient, and A_{eff} is the effective mode area.

To accurately model the effects of the nonlinear absorption, Eq. (1) is coupled to the equation for the free-carrier density N_c, which is given by:

$$\frac{\partial N_c(z,t)}{\partial t} = \frac{\beta_{\text{TPA}}}{2h\nu_0} \frac{|A(z,t)|^4}{A_{\text{eff}}^2} - \frac{N_c(z,t)}{\tau}, \tag{2}$$

where τ ($\tau = 10$ ns [13]) is the free carrier lifetime.

Finally, a useful metric from which to evaluate the performance of the FWM process is to calculate the conversion efficiency (CE), defined as the ratio between the signal power P_s and the power of the generated idler P_i as:

$$\text{CE} = 10 \times \log_{10} \frac{P_i}{P_s}, \tag{3}$$

where the powers are extracted from the pulse amplitudes generated via Eq. (1).

3. Structural design

Our starting point for designing the waveguides was to consider two different structures: strip waveguides formed from 220 nm SOI and rib waveguides formed from a thicker 500 nm SOI platform. Both structures can be defined using standard photolithography and etching techniques to produce waveguides with cross-sections, as illustrated in Fig. 2(a). In these figures, H is the thickness of the silicon on top of the insulator layer, h is the etch depth, and W is the width. The longitudinal waveguide design is the same in both cases, as depicted in the bottom image of Fig. 2(a), where a straight section is sandwiched between two coupling regions (a down and up taper) to ensure good coupling into the few hundred nanometer-sized waveguides. We note that although several of our waveguide designs support multiple guided modes, by optimizing coupling into the tapered regions it is possible to ensure that the fundamental mode is predominantly excited.

Of the two cross-section designs, the thicker waveguides are typically associated with lower propagation loss values, with strip waveguide losses often reported to be $\sim 2 - 4$ dB/cm and rib waveguides having loss values ~ 1 dB/cm [15]. However, there is another advantage of the rib structure in that by having access to two optimization parameters (width and etch depth) it is possible to have greater control of the dispersion properties. To illustrate this, Fig. 2(b) shows the second- and fourth-order dispersion parameters (β_2 and β_4, respectively), as calculated via modal analysis using COMSOL, for two waveguide designs with the dimensions of h = 350 nm and W = 790 nm for the rib, and W = 790 nm for the strip. These waveguide designs were chosen specifically so that the zero-dispersion wavelength (ZDW: $\beta_2 = 0$) is close to the desired pump wavelength of 1545 nm, and thus represent an optimum configuration for efficient FWM. Figure 2(c) then plots the FWM conversion efficiency for the two structures as a function of wavelength, as calculated via the NLSE using Matlab for a pump power of 100 mW, a signal power of 5 mW, and assuming the same loss value of 1 dB/cm. The propagation length was set to
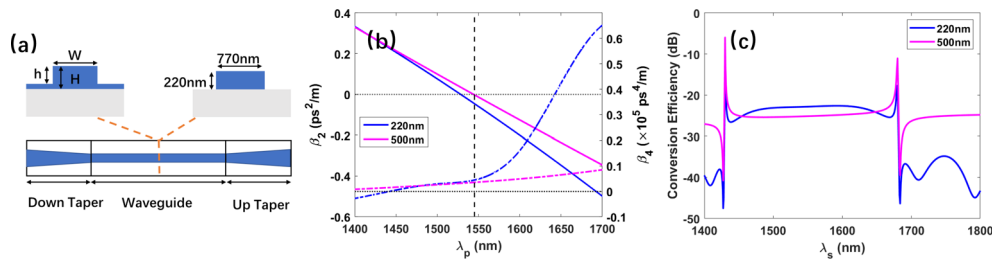
Fig. 2. (a) Structural diagram of the planar waveguide designs. The top two images depict cross-sections of a rib waveguide with the top silicon layer of 500 nm and strip waveguide with a top silicon layer of 220 nm. The bottom image shows the longitudinal variation including input and output coupling regions. Second- and fourth-order dispersion parameters (b) and FWM bandwidth (c) for the two optimized structures illustrated in (a).

1 cm to avoid the generation of higher-order Stokes and anti-Stokes light due to the accumulation of Raman gain with increasing propagation length. The sharp peaks seen on the conversion curves are due to RE-FWM, where the short-wavelength peak is associated with CSRS and the long-wavelength peak is CARS. It is clear from these results that there is a notable difference in the achievable FWM bandwidth, with the thicker 500 nm rib waveguide providing the better overlap with the Raman peaks to achieve a higher maximum gain (~ -6 dB). Thus, we fixed on the design of the rib structure in the 500 nm thick silicon, but continued to investigate the role of the width and etch depth to ensure the optimal design had been achieved.

Figure 3(a) plots the dispersion profile for various rib waveguide dimensions (h and W values) for the chosen pump wavelength of 1545 nm. As already mentioned, it is preferable to operate near the ZDW to obtain a broad and efficient FWM bandwidth, which is depicted by the black dash line. From this figure it is clear that the zero-dispersion condition can be achieved for different combinations of h and W, with larger widths simply corresponding to larger etch depths. Moreover, β_2 changes slowly along the width, but dramatically along the etch depth, which suggests that the dispersion profile is more sensitive to the critical dimension of waveguides. To illustrate the influence of the different waveguide dimensions, Fig. 3(b) shows conversion efficiencies for three different combinations of h and W as a function of the signal wavelength. As for Fig. 2(c), the simulations were conducted with a pump power of 100 mW, a signal power of 5 mW, a length of 1 cm, and loss value of 1 dB/cm. Again, the strong RE-FWM peaks are observed on the spectra, but this time they are all well positioned in the middle of the flat section of the bandwidth. Moreover, in all cases the CSRS is stronger than the CARS by a conversion efficiency of ~ 4 dB, which originates from the inherent higher energy transfer efficiency at the Stokes wavelength compared to the anti-Stokes wave. Therefore, CSRS is the focus in the following discussion about the performance of RE-FWM.

As seen in Fig. 3(b), the conversion efficiency for CSRS remains approximately stable for the different combinations of h and W. The bandwidth, defined as the signal wavelength range where the conversion efficiency drops by 3 dB from the maximum value at the centre of the curve, is largest for the etch depth of 350 nm. This is due to the difference in the values of β_2 and the corresponding values of β_4, which combine to minimise the total dispersion. Additionally, there is a trade-off between the effective mode area and the propagation loss caused by the interaction between the guided light and the sidewalls. As a result, we have settled on a target structure with h= 350 nm and W= 790 nm as a compromise between a small mode area to achieve a high mode intensity, but with the potential for low losses through a modest etch depth. This structure has dispersion values of $\beta_2 = -2.49 \times 10^{-3}$ ps^2/m and $\beta_4 = 3.53 \times 10^{-7}$ ps^4/m. In the
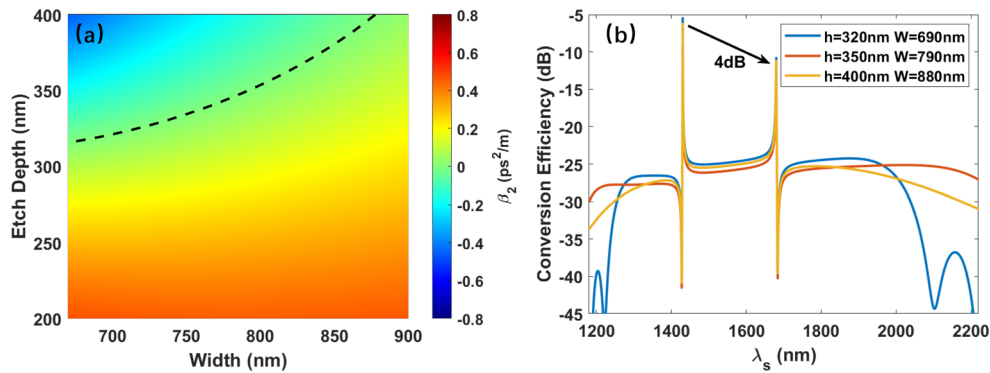
Fig. 3. (a) Second-order dispersion parameter (β_2) varying with etch depth (h) and width (W). The black dash line represents $\beta_2 = 0$. (b) Plot of conversion efficiency as a function of λ_s for waveguide designs with different combinations of h and W that have $\beta_2 = 0$ at the 1545 nm pump wavelength (i.e., the dimensions are selected from the black dash line in (a)). The simulations are conducted with a pump power of 100 mW, a signal power of 5 mW and a propagation length of 1 cm.

following simulations, the linear loss is assumed to be 1 dB/cm, based on typical values from our fabrication of waveguides from this platform [15].

4. Performance of CSRS

Following identification of the optimal structure, the influence of the structural parameters on the RE-FWM conversion efficiency was investigated to validate the design for the existing fabrication techniques. In these simulations, the system parameters are the same as those used for Fig. 3. Figure 4(a) displays the conversion efficiency as a function of λ_s as the etch depth h is changed from 280 nm to 420 nm. As expected, the bandwidth is at a maximum when h is equal to the optimum value of 350 nm, but decreases quite sharply as h is increased or decreased away from this. Figure 4(b) then shows the efficiency as the waveguide width W is changed from 670 nm to 900 nm. Again, the bandwidth is maximum for the designed width of 790 nm, but the rate of decrease of the bandwidth as the width is adjusted is less sharp than for the changing etch depth.

In both cases it is clear that CSRS, marked by the black dash boxes, is strongly excited when the bandwidth of FWM overlaps with the Raman gain spectrum. Figure 4(c) and Fig. 4(d) display the conversion efficiency as a function of h and W, which are extracted from Fig. 4(a) and 4(b), respectively. The reference conversion efficiency is set as −10 dB, as denoted by the dash lines in Fig. 4(c) and (d), which is around 4 dB less than the maximum conversion for the 100 mW pump. It is noteworthy that, even with a lower pump power and a larger effective mode area compared to the system previously used to report the highest FWM conversion efficiency [7], higher conversion efficiencies can be easily achieved via our geometry by coupling the nonlinear processes of FWM, SRS and IRS. Based on this reference value, we can determine the fabrication tolerance of the etch depth h to be 20 nm and width W to be 47 nm, which are well within the attainable resolutions for existing photolithography technologies [16]. The smaller structural tolerance of h compared with that of W is consistent with the dispersion analysis, which further confirms that the nonlinear performance is more sensitive to the smallest dimension of planar waveguides.

Having established the fabrication tolerances for this design, we subsequently investigated the performance of the RE-FWM by comparing the conversion efficiency and Stokes output power for the CSRS process. Figure 5(a) plots a colour map of the conversion efficiency as functions of
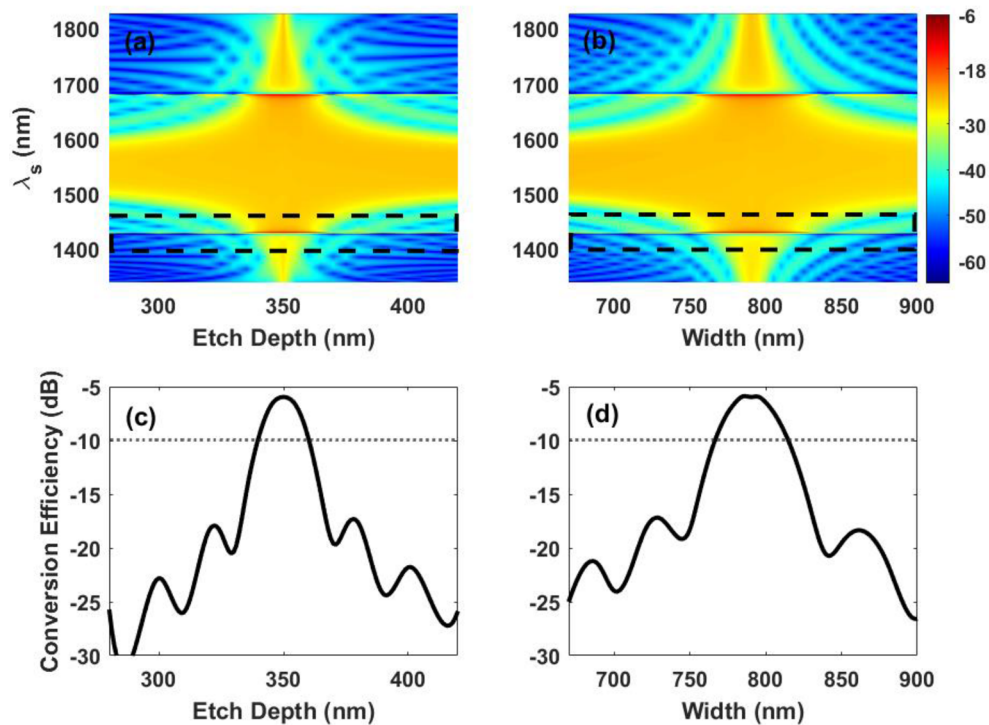
Fig. 4. (a) Conversion efficiency as functions of h and λ_s. (b) Conversion efficiency as functions of W and λ_s. (c) and (d) show the conversion efficiencies of the CSRS processes, marked with black dash boxes in (a) and (b), respectively, where signal is tuned to the anti-Stokes wavelength of 1430 nm. In all cases the pump wavelength is 1545 nm with a power of 100 mW, the signal power is 5 mW and the propagation length is 1 cm.

pump power and wavelength length, with the remaining parameters for the pump, signal and waveguide the same as used previously for Fig. 4. From this result we see that as the pump power increases above ∼ 200 mW, the conversion efficiency saturates at a propagation length of ∼ 3 cm. We attribute this saturation to the fact that for high pump powers the Stokes light is sufficiently enhanced to transfer energy to the anti-Stokes wave, as well as to higher order Stokes waves. As a result, the optimal pump power to achieve a maximum conversion efficiency of approximately 45 dB is only 130 mW, with a propagation length of 4.6 cm. We note that for such efficient conversion, the deviation between CSRS and CARS is increased to >50 dB, which reinforces the advantages of this pumping scheme. Although this pump power is higher than used in other studies of FWM [17,18], such powers are readily available within telecom systems and the advantage of our approach is that it only relies on a simple waveguide design, without the need for extremely low linear loss or ring resonator designs, to achieve an enhancement in the conversion efficiency of ∼ 50 dB. In fact, even in the case of higher linear losses ∼ 4 dB/cm, although the maximum conversion efficiency decreases to ∼ −0.5 dB, the enhancement of CSRS compared with pure FWM still reaches up to ∼ 21 dB.

Figure 5(b) then shows a colour map of the achievable Stokes output power as functions of pump power and waveguide length. It shows that the output idler power saturates for both increasing power and length, reaching a maximum of 560 μW for a 130 mW pump at a length of 3.2 cm. We attribute the saturation associated with increased power both to the conversion of the first order Stokes wave to higher order waves as well as nonlinear absorption associated with TPA and free-carrier effects. Thus, an effective way to improve the Stokes output power would
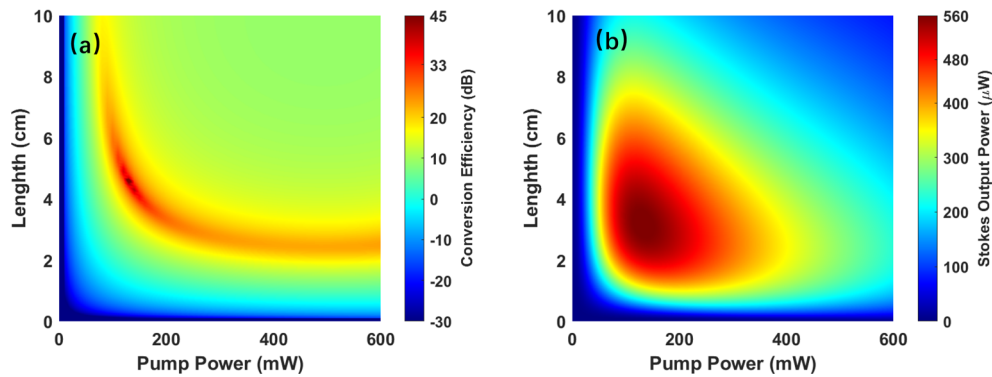
Fig. 5. (a) Conversion efficiency and (b) Stokes output power as functions of the pump power and waveguide length when pumping at 1545 nm with a 5 mW signal beam positioned at 1430 nm.

be to shift the pump wavelength beyond 2 μm, where the nonlinear absorption diminishes. In contrast, the saturation for increasing propagation length is primarily due to the linear loss, so that the Stokes output power could also be increased through further reduction of the transmission losses. Although the maximum Stokes power does not occur at the same length as the maximum conversion efficiency, it is worth noting the conversion efficiency is still as high as 14 dB in this instance. Therefore, a single waveguide could be used to achieve the maximum Stokes output power and considerable conversion efficiency. The inconsistency in the optimized propagation length for the maximum conversion efficiency and Stokes output power is attributed to the presence of IRS, which leads to a decrease in anti-Stokes wave power that appears in the efficiency calculation. This results in a slightly slower saturation of conversion efficiency as a function of propagation length. Comparing the maximum achieved Stokes power with previous reports for pure SRS, it is quite remarkable that the power generated using the RE-FWM scheme is 7 dB larger than what has been obtained in a waveguide of comparable length but with a p-i-n structure built in to reduce the free-carrier absorption [19]. Significantly, if we reduce the losses to 0.3 dB/cm in our simulations, which corresponds to the lowest linear loss for planar waveguides in the telecom band at this time [20], we can achieve idler powers up to 1.47 mW for a pump power of only 80 mW and a length of 10 cm.

5. Conclusion

In this work, we have explored optimum designs for planar waveguide structures to exploit RE-FWM processes in the telecom band. For a pump at 1545 nm, a rib structure formed from a 500 nm thick SOI platform with an etch depth of 350 nm and a width of 790 nm was found to provide a good compromise between achieving a good overlap between the gain bandwidths of the nonlinear processes, but with potential for low propagation losses. Moreover, the design was shown to have good fabrication tolerance to achieve strong conversion efficiencies even with variations of 20 nm or more in the waveguide parameters. A maximum conversion efficiency of $\sim$ 45 dB could be obtained with a pump power of 130 mW over a propagation length of 4.6 cm, which is over 50 dB higher than typical reports of FWM in silicon planar waveguides. Applying the same pump power, a maximum Stokes power of over 560 μW could be achieved within a slightly shorter length of 3.2 cm, and additional simulations have shown that the output power could be increased further by reducing the losses to less than 1 dB/cm. The design principle illustrated in this paper allows for the application potential of RE-FWM to be explored at any desired wavelength by optimizing the structure to achieve the maximum required output. Thus,

we expect the high conversion efficiencies and large Stokes output powers that can be generated through RE-FWM processes could be exploited in wide ranging areas extending well beyond traditional signal processing and communications applications.

Disclosures. The authors declare no conflicts of interest.

Data availability. Data underlying the results presented in this paper are available in Ref. [21].

References

1. H. Fukuda, K. Yamada, T. Shoji, *et al.*, "Four-wave mixing in silicon wire waveguides," Opt. Express **13**(12), 4629–4637 (2005).
2. Y.-H. Kuo, H. Rong, V. Sih, *et al.*, "Demonstration of wavelength conversion at 40 gb/s data rate in silicon waveguides," Opt. Express **14**(24), 11721–11726 (2006).
3. R. Salem, M. A. Foster, A. C. Turner, *et al.*, "Signal regeneration using low-power four-wave mixing on silicon chip," Nat. Photonics **2**(1), 35–38 (2008).
4. Y. Cao, L. Zhang, Y. Fei, *et al.*, "Effect of frequency chirp on supercontinuum generation in silicon waveguides with two zero-dispersion wavelengths," Opt. Commun. **334**, 190–195 (2015).
5. J. R. Ong, R. Kumar, R. Aguinaldo, *et al.*, "Efficient cw four-wave mixing in silicon-on-insulator micro-rings with active carrier removal," IEEE Photonics Technol. Lett. **25**(17), 1699–1702 (2013).
6. J. R. Ong, M. L. Cooper, G. Gupta, *et al.*, "Low-power continuous-wave four-wave mixing in silicon coupled-resonator optical waveguides," Opt. Lett. **36**(15), 2964–2966 (2011).
7. M. A. Foster, A. C. Turner, R. Salem, *et al.*, "Broad-band continuous-wave parametric wavelength conversion in silicon nanowaveguides," Opt. Express **15**(20), 12949–12958 (2007).
8. W. M. Tolles, J. W. Nibler, J. McDonald, *et al.*, "A review of the theory and application of coherent anti-stokes raman spectroscopy (cars)," Appl. Spectrosc. **31**(4), 253–271 (1977).
9. R. Claps, V. Raghunathan, D. Dimitropoulos, *et al.*, "Anti-stokes raman conversion in silicon waveguides," Opt. Express **11**(22), 2862–2872 (2003).
10. T. Sylvestre, H. Maillotte, E. Lantz, *et al.*, "Raman-assisted parametric frequency conversion in a normally dispersive single-mode fiber," Opt. Lett. **24**(22), 1561–1563 (1999).
11. S. Sun, M. Huang, D. Wu, *et al.*, "Raman enhanced four-wave mixing in silicon core fibers," Opt. Lett. **47**(7), 1626–1629 (2022).
12. L. Yin, Q. Lin, and G. P. Agrawal, "Soliton fission and supercontinuum generation in silicon waveguides," Opt. Lett. **32**(4), 391–393 (2007).
13. R. Claps, V. Raghunathan, D. Dimitropoulos, *et al.*, "Influence of nonlinear absorption on raman amplification in silicon waveguides," Opt. Express **12**(12), 2774–2780 (2004).
14. L. Zhang, A. M. Agarwal, L. C. Kimerling, *et al.*, "Nonlinear group iv photonics based on silicon and germanium: from near-infrared to mid-infrared," Nanophotonics **3**(4-5), 247–268 (2014).
15. C. G. Littlejohns, D. J. Rowe, H. Du, *et al.*, "Cornerstone's silicon photonics rapid prototyping platforms: Current status and future outlook," Appl. Sci. **10**(22), 8201 (2020).
16. S. Saharan, B. Yadav, A. Grover, *et al.*, *Fabrication Methods for Bio-MEMS* (IGI global, 2023).
17. M. Ding, M. Zhang, S. Hong, *et al.*, "High-efficiency four-wave mixing in low-loss silicon photonic spiral waveguides beyond the singlemode regime," Opt. Express **30**(10), 16362–16373 (2022).
18. J. Hong, K. Rokumyo, J. Mao, *et al.*, "Efficient four-wave mixing wavelength conversion in a hybrid silicon slot and polymer microring resonator," Opt. Express **30**(25), 45499–45507 (2022).
19. M. Ahmadi, J. Lefebvre, W. Shi, *et al.*, "Non-reciprocal sub-micron waveguide raman amplifiers, towards loss-less silicon photonics," IEEE J. Sel. Top. Quantum Electron. **29**, 1–9 (2022).
20. S. Y. Siew, B. Li, F. Gao, *et al.*, "Review of silicon photonics technology and platform development," J. Lightwave Technol. **39**(13), 4374–4389 (2021).
21. S. Sun, G. Z. Mashanovich, and A. C. Peacock, "Dataset supporting the publication "design of integrated silicon waveguides for raman-enhanced four-wave mixing in the telecom band"," University of Southampton (2023). https://doi.org/10.5258/SOTON/D2816.